# Airborne remote sensing of Arctic boundary-layer mixed-phase clouds

**André Ehrlich, Eike Bierwirth, Manfred Wendisch**

## Summary

This article gives an overview on the investigations on Artic boundary-layer mixed-phase clouds conducted within the Arctic Study of Tropospheric Aerosol, Clouds and Radiation (ASTAR) in spring 2007. In particular the horizontal and vertical disribution of ice crystals within the clouds was determined by three independent airborne instruments (lidar, in situ and solar radiation measurements).
Spectral measurements of cloud top reflectivity have been utilized to retrieve information on the ice phase by analyzing the spectral pattern of the cloud top reflectance in the wavelength range dominated by liquid water and ice absorption (1400-1700 nm). A new algorithm to derive an ice index which distinguishes pure ice, liquid water, and mixed-phase clouds was developed. The horizontal distribution of the ice index, observed during ASTAR 2007, agrees with airborne lidar and in situ measurements showing patches of glaciated clouds at an air mass transition zone within the investigated mixed-phase cloud fields.
Information on the vertical distribution of ice crystals in mixed-phase clouds was derived by comparing the measured cloud top reflectivity in the wavelength band 1400-1700 nm to radiative transfer simulations. To interpret the data, the vertical weighting of the measurements was calculated. In the investigated wavelength range the weightings differ according to the spectral absorption of ice and liquid water. From the observed spectral cloud reflectivity with low values in the ice absorption maximum (1400 nm) and higher values at the liquid water absorption maximum (1700 nm) it was concluded that ice crystals were present in the otherwise liquid dominated cloud top layer. Although in situ measurements (limited due to vertical resolution and detection limits) did confirm these findings only in certain limits, the retrieved vertical structure is in agreement with published ground based remote sensing measurements.

## 1 Arctic boundary-layer mixed-phase clouds

Mixed-phase clouds are common in the Arctic due to low temperatures. In particular, Arctic boundary-layer mixed-phase (ABM) clouds form above open sea in conjunction with cold air outbreaks. They consist of both, supercooled liquid water particles and solid ice crystals simultaneously, and were observed and investigated during numerous Arctic field experiments (e.g., Turner et al., 2003, Verlinde et al., 2007, Shupe et al., 2008).
The persistent coexistence of ice crystals (ice water content, $IWC$) and liquid water particles (liquid water content, $LWC$) in these clouds relies on the balance between the condensation rate of liquid water droplets ($LWC$ rate), the ice crystal growth rate ($IWC$ rate), and the removal of ice nuclei (IN) by precipitating ice crystals. Such a basic scheme was introduced by (Harrington et al., 1999) and is displayed in Figure 1.
The unstable temperature layering above the open sea induces convection by which liquid water nucleation occurs in the updrafts (increase of $LWC$). As the concentration of cloud condensation nuclei (CCN) is typically lower than the concentration of IN (*e.g.*, Fridlind et al., 2007, Morrison et al., 2008), the liquid water nucleation exceeds the ice crystal nucleation in this part

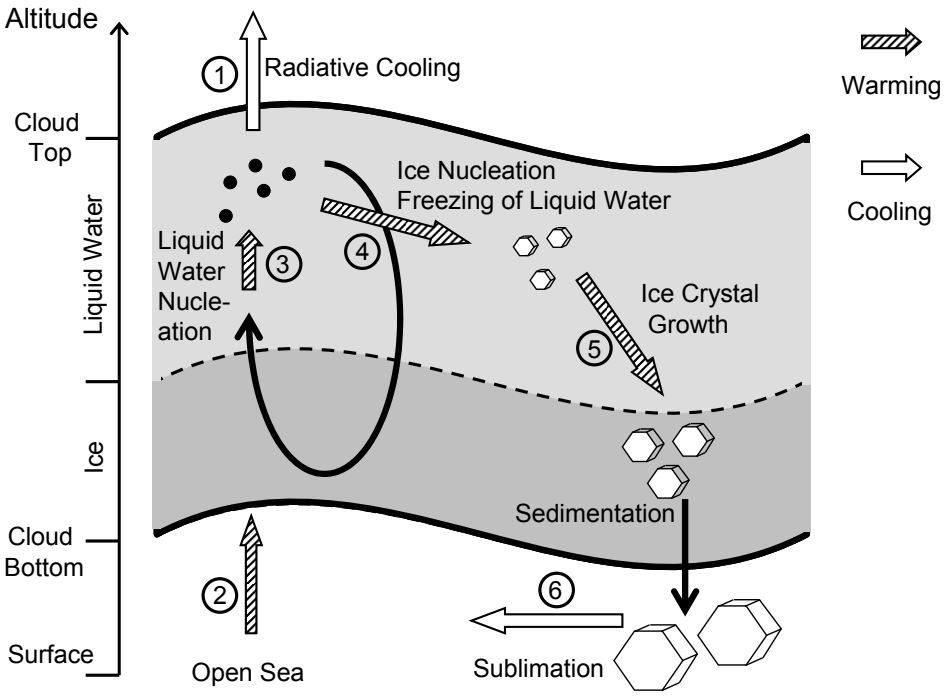


Figure 1: Illustration of the relevant processes present in ABM clouds. Processes that cause a cooling of the surrounding air are indicated by empty arrows; processes which lead to a warming are plotted with filled arrows.

of the cloud ($LWC$ rate $>$ $IWC$ rate). However, once ice crystals have formed from IN or by freezing of liquid water droplets, they grow due to the Wegener-Bergeron-Findeisen mechanism at the expanse of the liquid water droplets. Finally, the ice crystals start to sediment which removes ice mass (decrease of $IWC$) and IN from the cloud system. The removal of IN due to the precipitating ice crystals reduces the ice crystal number concentration and prevents for total glaciation of the ABM clouds.
However, this equilibrium state is unstable. Slight changes might shift the fractional ice and liquid water component drastically (e.g. Morrison et al., 2008, Fan et al., 2008, Harrington et al., 1999). The radiative impact of such phase transitions in Arctic mixed-phase clouds was investigated by Ehrlich (2009) and Ehrlich et al. (2008b) using radiative transfer simulations. The local and temporary radiative forcing $\mathcal{F}_\Delta$ of an exemplary Arctic boundary-layer mixed-phase cloud was simulated in dependance of its ice volume fraction $f_\mathrm{I}$ which is defined by the ratio of $IWC$ to total water content $TWC$,

$$f_\mathrm{I} = \frac{IWC}{TWC}. \tag{1}$$

If a mixed-phase clouds glaciates into a pure ice cloud, which is consistent to an increase of $f_\mathrm{I}$ for constant $TWC$, the cloud optical thickness decreases due to the larger size of the ice crystals compared to the smaller liquid water droplets. The result is an decrease of the clouds radiative impact as shown in Figure 2. The simulations shown here are performed for a solar zenith angle of $\theta_0 = 71°$ and a typical ABM cloud with a total water path of $TWP = 100\,\mathrm{g\,m^{-2}}$, an ice crystal effective diameter of $D^\mathrm{I}_\mathrm{eff} = 90\,\mu\mathrm{m}$ and water droplets with effective diameter of $D^\mathrm{W}_\mathrm{eff} = 15\,\mu\mathrm{m}$. For both, surface and top of the atmosphere, $\mathcal{F}_\Delta$ increases significantly about $90\,\mathrm{W\,m^{-2}}$ with increasing $f_\mathrm{I}$. This means that the cooling of the clouds is reduced when a

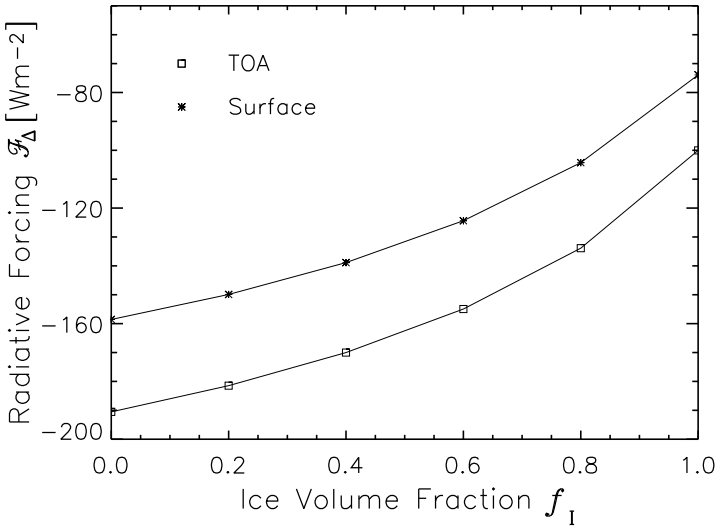


Figure 2: Radiative forcing $\mathcal{F}_\Delta$ of mixed-phase clouds calculated for the top of atmosphere (TOA) and the surface. The state of mixing was varied using $f_\mathrm{I}$ with $TWP = 100\,\mathrm{g\,m^{-2}}$, $D_\mathrm{eff}^\mathrm{I} = 90\,\mu\mathrm{m}$ and $D_\mathrm{eff}^\mathrm{W} = 15\,\mu\mathrm{m}$.

transition from liquid or mixed-phase to pure ice clouds occurs.
The investigations published by Ehrlich (2009) and Ehrlich et al. (2008b) have shown that knowledge on the thermodynamic state (liquid water, mixed-phase or ice) of clouds is essential to determine their radiative impact. On a global scale, satellite measurements are currently the only option to characterize clouds in this regard. Similar remote sensing techniques using airborne solar radiation measurements will be described in the following sections.

# 2 Airborne Measurements

Airborne measurements to characterize ABM clouds were obtained during the Arctic Study of Tropospheric Aerosol, Clouds and Radiation (ASTAR) 2007 campaign. The campaign took place in the vicinity of Svalbard (78° N, 15° E) in March/April 2007 and focused on the sampling of ABM clouds.
During ASTAR 2007 the POLAR 2 aircraft, owned by the Alfred Wegener Institute for Polar and Marine Research (AWI), Bremerhaven, Germany, was equipped to probe clouds with airborne remote-sensing and in situ instruments. The Spectral Modular Airborne Radiation measurement sysTem (SMART) albedometer, the Airborne Mobile Aerosol Lidar (AMALi) and in situ instruments such as Polar Nephelometer, Cloud Particle Imager (CPI), and Particle Measuring System (PMS) Forward Scattering Spectrometer Probe (FSSP-100), operated on Polar 2, have been described in detail by Ehrlich (2009), Lampert et al. (2009a) and Gayet et al. (2009), respectively.
The SMART-Albedometer was used to perform remote sensing measurements using solar radiation (Wendisch et al., 2001, Bierwirth et al., 2009). The specific configuration of the SMART-Albedometer, operated during ASTAR 2007, has been introduced in detail by Ehrlich et al. (2008a). It provides measurements of downwelling and upwelling spectral irradiances ($F_\lambda^\downarrow$, $F_\lambda^\uparrow$) simultaneously with upwelling nadir spectral radiance ($I_\lambda^\uparrow$). These data were used to calculate spectral cloud-top reflectivities $R$ in the wavelength range between 350 nm and 2150 nm by,

$$R(\lambda) = \frac{\pi\,\mathrm{sr} \cdot I_\lambda^\uparrow}{F_\lambda^\downarrow}. \tag{2}$$

In this definition $F_\lambda^\downarrow$ includes diffuse and direct solar radiation and is measured with respect to a horizontal plane $F_\lambda^\downarrow = F_\lambda^\downarrow(\cos\theta)$ with $\theta$ being the solar zenith angle. The spectral resolution of $R(\lambda)$ (full width at half maximum, FWHM) amounts to 2–3 nm in the wavelength range 350–950 nm and 9-16 nm for $\lambda = 950$–2150 nm wavelength.

AMALi is a two-wavelength (532 nm and 355 nm) backscatter lidar with depolarization measurements at 532 nm wavelength. For cloud observations, AMALi was installed in nadir-looking configuration. The vertical resolution was 7.5 m; the minimum horizontal resolution was about 900 m. The depolarization ratio derived from the 532 nm wavelength channel allows to distinguish lidar backscatter signals of ice crystals from those of liquid water droplets.

The in situ measurements of cloud microphysical properties include particle number size distribution in the size range of 3-27 $\mu$m for the FSSP and 23-2300 $\mu$m for the CPI, extinction coefficient, ice and liquid water content and effective diameter. The Polar Nephelometer provides the scattering phase function and the asymmetry parameter, a measure for the anisotropy of the scattering phase function.

The data of all three instruments have been used to derive information on the horizontal and vertical distribution of ice crystals in ABM clouds.

# 3 Horizontal distribution of ice

## 3.1 Methodology

The characteristics of the spectral reflectivity measurements of the SMART-albedometer were utilized in three different approaches to retrieve the cloud thermodynamic phase (pure liquid, mixed-phase and pure ice cloud). Two ice indices were calculated based on the differences in the spectral absorption of ice and liquid water. Therefore, a known two-wavelengths approach (spectral slope ice index) and a principle component analysis (PCA ice index) was applied. A third approach used the different scattering characteristics of ice crystals and liquid water droplets and combined albedo and reflectance measurements to obtain information on the cloud phase (anisotropy ice index). A detailed description of the methodology and a discussion on the applicability of these ice indices have been published in Ehrlich et al. (2008a).

The dimensionless spectral Slope Ice Index $I_\mathrm{S}$ was adapted from Acarreta et al. (2004) to the specifications of the SMART-albedometer using the wavelength range between $\lambda_a = 1550$ nm and $\lambda_b = 1700$ nm and is defined by,

$$I_\mathrm{S} = 100 \cdot \frac{\lambda_b - \lambda_a}{R_{1640}} \cdot \left[\frac{\mathrm{d}R}{\mathrm{d}\lambda}\right]_{[\lambda_a,\lambda_b]} \tag{3}$$

Typical values for liquid water clouds range between $I_\mathrm{S} = 5$ and $I_\mathrm{S} = 15$. Ice clouds show a higher variability of $I_\mathrm{S}$ with values of up to 80.

The PCA ice index $I_\mathrm{P}$ utilizes the principle components of the reflectivity measurements which are related to ice $PC_\mathrm{I}$ and liquid water absorption $PC_\mathrm{W}$. The dimensionless index is defined as,

$$I_\mathrm{P} = \left(\frac{PC_\mathrm{I}}{PC_\mathrm{W}} - 0.94\right) \cdot 100. \tag{4}$$

The offset of 0.94 has been determined arbitrarily in order to obtain values close to zero for liquid water clouds ($I_\mathrm{P} = 0$–1). For ice clouds, $I_\mathrm{P}$ ranges from values of 1 up to 8 clearly capable of being distinguished from liquid water clouds.

Sensitivity studies have shown that both indices, $I_\mathrm{S}$ and $I_\mathrm{P}$, are most sensitive to the upper cloud layer. Further, their values depend strongly on the ice particle effective diameter and less on the cloud optical thickness for $\tau < 5$. Nevertheless, an ambiguity in the discrimination of

ice and liquid water phase occurs only between pure ice clouds with small ice crystals and low $\tau$, and pure liquid water clouds of high $\tau$. More crucial is the dependence on the ice particle effective diameter for the discrimination between mixed-phase and pure ice clouds. Here, *a priori* knowledge about the ice crystal dimensions is required.

Independently, the particle phase was determined from in situ data, based on the combination of asymmetry parameter and particle number concentration measurements (Gayet et al., 2009). As an approximation it was defined that the FSSP (size range 3–27 $\mu$m) measured liquid water droplets, whereas the CPI (23–2 300 $\mu$m) was used to determine the size distribution of large ice crystals. This assumption is based on the ice crystals sizes expected for mixed-phase conditions (*e.g.*, Korolev et al., 2003, Shupe et al., 2006). Due to the WBF process, the ice crystals rapidly grow to sizes larger than the range covered by the FSSP. This assumption was justified by simultaneous polar nephelometer measurements of the asymmetry parameter $\langle g \rangle$ (Ehrlich, 2009). The analysis of the data showed that the majority of the FSSP measurements coincide with $\langle g \rangle = 0.84$–0.86 indicating liquid water droplets. The CPI measured high particle number concentrations where the asymmetry parameter indicates nonspherical ice crystals ($\langle g \rangle = 0.78$–0.80).

The laser of the AMALi lidar did not completely penetrate the optically thick clouds. However, AMALi did identify a liquid water layer at cloud top by the depolarization signal (Lampert et al., 2009a). Although multiple scattering in the liquid water layer generated high depolarization values, comparable to the depolarization signal of ice crystals, the detailed analysis of the lidar profiles averaged over 15 seconds reveals differences in the vertical pattern of the depolarization. The depolarization related to multiple scattering of liquid water particles increases slowly with cloud depth whereas nonspherical ice crystals result in an instantaneous increase of the depolarization (Hu et al., 2007). From this analysis the precipitating ice below the clouds was identified in several cloud gaps.

## 3.2 Case Study on April 9, 2007

On April 9, 2007 concurrent radiation and microphysical measurements have been conducted along the path of the Cloud-Aerosol Lidar and Infrared Pathfinder Satellite (CALIPSO) over the Greenland Sea as marked in Figure 3. A stratus cloud field with cloud top up to 2000 m extended above the open ocean west to Svalbard. Due to the weakened advective supply of cold air from the northern sea ice, the cloud field was characterized by heterogenous structures which are related to an air mass intersection (Gayet et al., 2009, Lampert et al., 2009b).

The profile of the total attenuated backscatter signal measured by CALIPSO is shown in Figure 4a and displays distinct cloud patches with different cloud top altitudes and vertical thicknesses. The cloud top altitude tends to increase towards North what is confirmed by the AMALi measurements. Between 78.7° N and 78.9° N a larger cloud gap has been observed. The cloud top is indicated by slightly enhanced depolarization signal of AMALi. Multiple scattering by the liquid water droplets at the cloud top layer leads to depolarization of the polarized radiation emitted by the AMALi laser. This layer with slightly enhanced

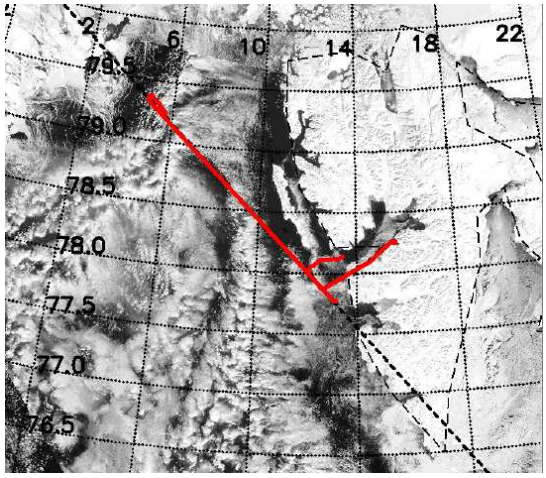


Figure 3: MODIS satellite image of April 9, 2007 overlaid with the flight track of POLAR 2 (red line) along the CALIPSO overpass (dashed black line). Numbers give the latitude and longitude respectively.

depolarization shows approximately the cloud top.

High depolarization ratios have been observed by AMALi between 78.5° N and 78.6° N and at about 79.0° N. The high depolarization indicates the presence of ice crystals. These areas coincide with high ice indices derived from the SMART-Albedometer measurements. Therefore, these cloud parts are identified as pure ice clouds. The in situ instruments did probe solely the ice cloud at 79.0° N. Here, ice crystal number concentrations up to $N_{\mathrm{tot}} = 4\,\mathrm{cm}^{-3}$ were measured. Although in situ measurements were taken at lower parts of this cloud, the remote sensing measurements reveal that the ice crystals were present up to the cloud top (Gayet et al., 2009).

The southern ice cloud was not completely sampled by the in situ measurements as the cloud top was significant lower at this location compared to the clouds observed in the surrounding area. The interruption of the cloud structure is visible at 78.5° N in the MODIS image taken at 10:00 UTC short before to the CALIPSO overpass (Figure 3). The lower cloud top and the ice crystals identified by the remote sensing instruments indicate that this part of the cloud mainly consists precipitating ice crystals which potentially have their origin in the surrounding clouds. South to 78.4° N the comparison of CALIPSO, in situ and remote sensing measurements fails due to the long time difference between the measurements. At the location between 78.2° N and 78.4° N a large cloud gap has been observed by CALIPSO and in situ instruments while the AMALi and SMART-Albedometer measurements indicate mixed-phase clouds with liquid cloud top layer.

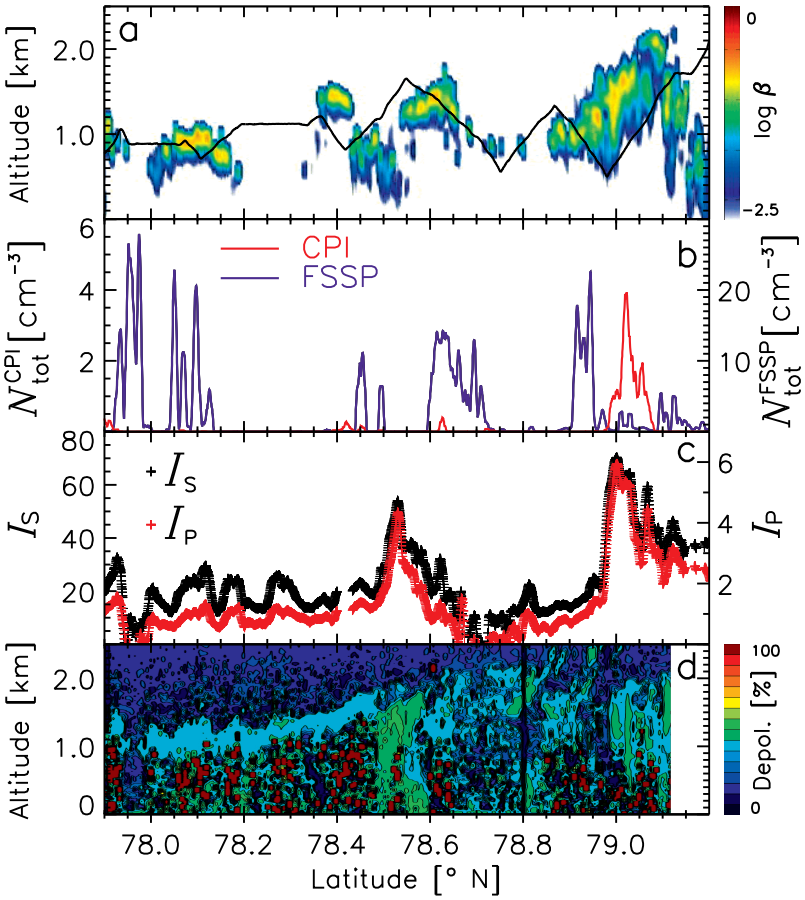


Figure 4: Profile of total attenuated backscatter coefficient $\beta$ [$\mathrm{sr}^{-1}\,\mathrm{km}^{-1}$] measured by CALIPSO in the cloud observed on April 9th (a). The flight track of the in situ measurements is overlaid as a black line. Ice and liquid water particle number concentrations $N_{\mathrm{tot}}$ measured by CPI and FSSP along the flight track and the ice indices $I_{\mathrm{S}}$ and $I_{\mathrm{P}}$ for the same positions are given in panel b and c. The depolarization profile obtained from AMALi is given in panel d.

# 4 Vertical distribution of ice

All three types of measurement on board of Polar 2 (in situ, lidar and solar radiation) provide a view on the vertical distribution of ice crystals in ABM clouds. By ascents into the cloud layer vertical profiles of ice crystal and liquid water droplet concentration were obtained by the in situ instrumentation (Gayet et al., 2009).

A typical profile of measured particle number concentrations, asymmetry parameters, liquid $LWC$ and ice water content $IWC$ obtained on April, 7 2007 is given in Figure 5. The FSSP indicated particle concentrations and $LWC$ up to $N_{\mathrm{tot}}^{\mathrm{FSSP}} = 50\,\mathrm{cm}^{-3}$ and $LWC = 115\,\mathrm{mg\,l}^{-l}$ between 1000–1700 m altitude. In the same layers the asymmetry parameter, measured by the Polar Nephelometer, was about 0.85 which is a typical value for spherical liquid water droplets (*e.g.*, Gerber et al., 2000, Garrett et al., 2001). A thin layer dominated by ice crystals was found between 800 m and 1100 m indicated by lower asymmetry parameters. In this layer the CPI measured particle number concentrations of up to $N_{\mathrm{tot}}^{\mathrm{CPI}} = 1.5\,\mathrm{cm}^{-3}$ with maximum particle dimensions of up to 1000 $\mu$m. Although the ice crystal number concentration is about a magnitude lower than the liquid water droplet concentration the ice crystals dominate the total water content with $IWC = 70\,\mathrm{mg\,l}^{-l}$. Below this layer, precipitating large ice particles have been observed down to 500 m by visual observation on board the aircraft and from in situ measurements (low ice water content and asymmetry parameter).

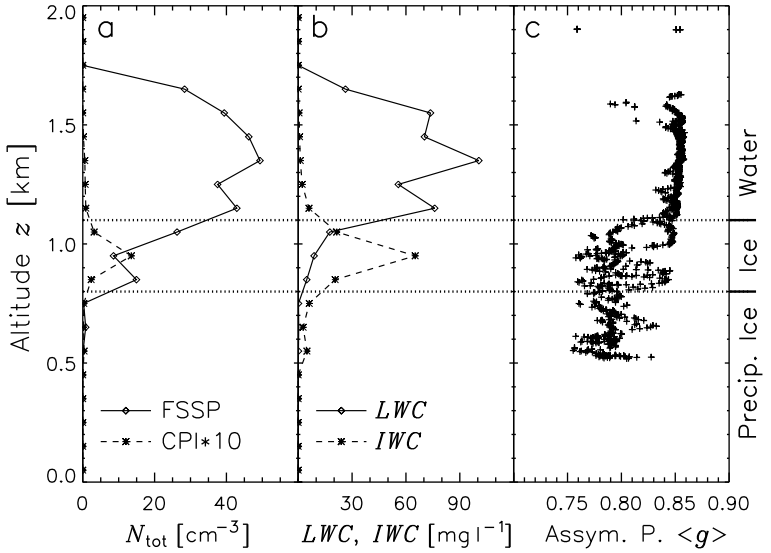


Figure 5: Profile of microphysical measurements obtained on April 7, 2007. Total particle number concentration $N_{\mathrm{tot}}$ measured by FSSP and CPI are given in panel a; $LWC$ and $IWC$ in panel b. The volumetric asymmetry parameter $\langle g \rangle$ obtained from the Polar Nephelometer is shown in panel c.

This vertical structure is typical for the Arctic stratus clouds, observed during ASTAR 2007, and was confirmed by detailed analysis of AMALi measurements (Lampert et al., 2009a). Although the lidar signal did penetrate the clouds layer only in cloud gaps with low optical thickness, a layer dominated by liquid water droplets was found at cloud top while precipitating ice crystals were observed in the cloud gap.

## 4.1 Vertical weighting functions

Independently, the vertical distribution of the ice crystals was estimated from the SMART-Albedometer measurements by comparison with radiative transfer simulations (Ehrlich et al., 2009). Therefore, the vertical weighting functions $W(z)$ of the reflectivity measurements in the

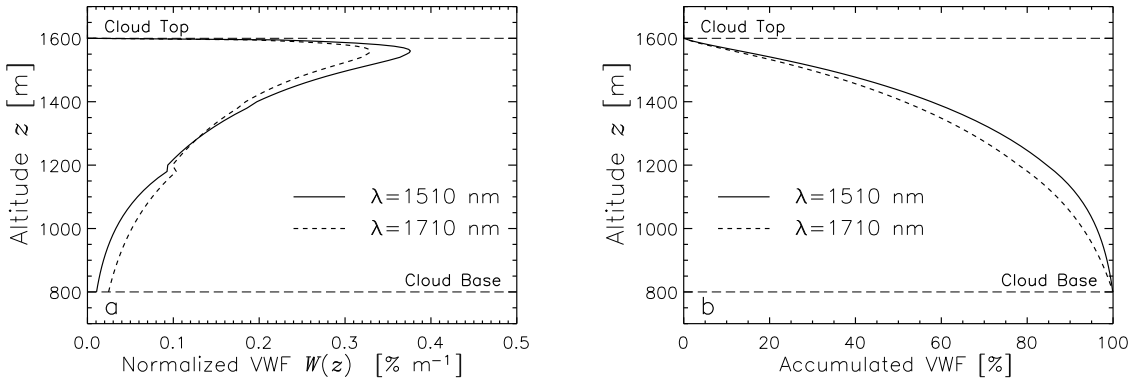


Figure 6: Vertical weighting function $W(z)$ for the radiance measurements of the SMART-Albedometer with respect to absorption by cloud particles (panel a). The accumulated weighting is given in panel b.

wavelength range dominated by ice and liquid water absorption (1300–1800 nm) were calculated by methods described by Platnick (2000).
The calculated $W(z)$ in units of [% m$^{-1}$] referring to the geometrical thickness of the cloud are given in Figure 6a for two wavelengths exemplary for strong ice (1510 nm) and liquid absorption (1710 nm). In Figure 6b $W(z)$ is accumulated over altitude starting with 0 % at cloud top. For both wavelengths, the weighting shows the highest contribution for cloud layers close to cloud top at 1550 m altitude. The maximum values of $W(z)$ are found to be higher for $\lambda = 1510$ nm than for $\lambda = 1710$ nm. With the higher values of $W(z)$ the cloud-top reflectivity at $\lambda = 1510$ nm is more dominated by absorption by particles at cloud top than $R$ at $\lambda = 1710$ nm. Therefore, $R$ at $\lambda = 1510$ nm is more suitable to retrieve the particle size at cloud top.
These spectral differences in $W(z)$ provide a tool to retrieve information on the vertical distribution of the cloud particle effective diameter, as described by Chen et al. (2007). Wavelengths where liquid water and ice absorption are strong can be used to derive particle properties at cloud top, whereas wavelengths with weaker absorption give information on particles located at lower cloud layers. Utilizing the spectral differences between the maxima of ice and liquid water absorption, separate vertical profiles for ice crystals and liquid water droplets can be derived.

## 4.2 Radiative transfer simulations

In this regard, radiative transfer simulations of cloud reflectivities have been performed for different vertical cloud geometries and compared to the measurements. Here the three most suitable cases out of those presented by Ehrlich et al. (2009) are shown. A cloud adapted to the vertical structure observed by the in situ instruments was simulated in Case A with an ice crystal layer topped by a liquid water layer (ice crystals in the upper cloud layer are neglected). In Case E a thin ice layer is situated adjacent to cloud top within the original cloud (mixed-phase cloud top); for Case F a thin ice layer is added above cloud top.
The spectral cloud-top reflectivity $R$ simulated for the cases A, E, and F is shown in Figure 7. The measurements of $R$ show that for wavelengths below $\lambda = 1700$ nm stronger absorption is measured than shown by the simulation of Case A. The maximum differences overlap with the ice absorption maximum ($\lambda = 1490$ nm). At wavelengths between 1700–1800 nm weaker absorption is observed.
Following the findings discussed above, the strong absorption at $\lambda = 1490$ nm implies that ice crystals of large effective diameter are present in the upper cloud layers. On the other hand,

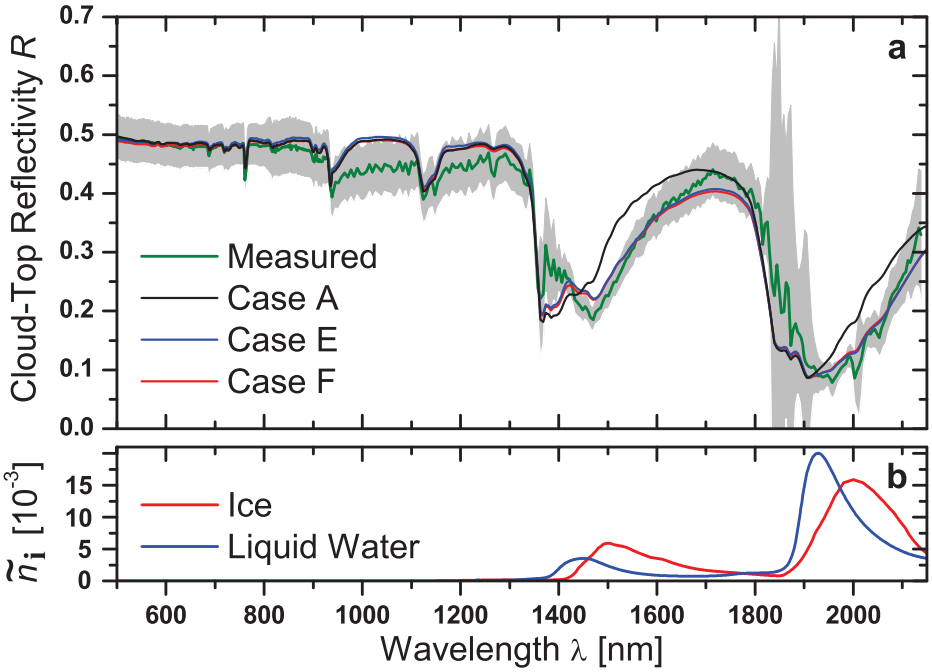


Figure 7: Measured and simulated spectral cloud-top reflectivity $R$ for cases A, E and F (panel a). The measurement uncertainty is illustrated by the gray area. In Panel b shows the refractive index $\tilde{n}_i$ of liquid water (Wieliczka et al., 1989) and ice (Warren and Brandt, 2008).

the high values of $R$ between 1700–1800 nm wavelength indicate cloud particles with smaller effective diameter at cloud top and at lower cloud layers. For cases E and F which have almost identical results these simulations fit into the uncertainty range of the observed $R$ at all wavelengths. Especially the spectral pattern in the wavelength range dominated by ice and liquid water absorption is closer to the measurements than simulations without additional ice layer. This reveals that ice crystals situated at cloud top are necessary to explain the observed absorption features with strong absorption at 1490 nm and weak absorption at wavelengths about 1750 nm. It has to be stated that this holds only for ice crystals of large effective diameter which, if added, describe the observed ice absorption in the measurements. Ice crystals of small effective diameter in low concentration which do not contribute as strongly to the ice absorption might be located throughout the cloud.

Further simulations analyzed the observation of backscatter glories during ASTAR 2007 which generally indicates the presence of liquid water droplets at cloud top. Implementing ice crystals directly within the uppermost cloud layer (Case E) reproduced a weak but visible backscatter glory and explains the observations. Situating the thin ice layer above the original cloud (Case F) eliminated the backscatter glory. From this analysis it is concluded that Case E rather than Case F does suit the remote-sensing observation above ABM clouds obtained during ASTAR 2007.

# 5 Conclusion and outlook

Airborne measurements with three different core instruments including solar radiation, in situ and lidar measurements were conducted during the ASTAR 2007 campaign to investigate Arctic boundary-layer mixed-phase clouds. Each instrument provided independent information on the horizontal and vertical distribution of ice crystals and liquid water droplets in these clouds.
For the remote sensing measurements of solar radiation new methods have been developed to determine the cloud phase and the vertical distribution of ice crystals. The spectral measurements in the wavelength range 1500–1700 nm where absorption of radiation by ice and liquid water is evident was found to be suitable to retrieve these information.
Case studies of ASTAR 2007 have shown that the horizontal distribution of cloud phase can be highly inhomogeneous especially if the extended cloud fields are disturbed by changing meteorological conditions. This might have a non-negligible impact on the 3-dimensional radiative transfer within this clouds.
Further, the vertical structure of the ABM clouds was identified by all three instruments. Basically the data showed a cloud top layer dominated by liquid water and a lower cloud layer dominated by ice crystals. In more detail the solar radiation measurements indicated that ice crystals were also present in the upper layers of the observed clouds. Analysis of the in situ and lidar measurements could neither confirm nor reject these results. The absence of ice crystals in the in situ measurements at cloud top is probably due to the flight strategy (vertical profiling) providing only short passages of this cloud layer and the horizontal variability of ABM clouds as shown by Gayet et al. (2009). The lidar measurements are highly affected by multiple scattering processes and are not suitable to detect few ice crystals within numerous liquid water droplets. However, similar clouds have been investigated by McFarquhar et al. (2007), Shupe et al. (2006, 2008) who confirmed the presence of ice crystals throughout the entire clouds by in situ and ground-based measurements.
Based on the proof of concept studies shown here, further investigations on the horizontal distribution of ice and liquid water in mixed-phase clouds are planned. Therefore, airborne measurements will be conducted within the study on Solar Radiation and Phase Discrimination of Arctic Clouds (SORPIC) in April/May 2010. The core instruments operated on the Polar 2 aircraft during ASTAR 2007 will be installed on the new Polar 5 aircraft of AWI. Additionally, a sun photometer, polarized solar radiance measurements, and the hyperspectral camera system AISA Eagle will be integrated on Polar 5 during SORPIC.
The in situ and remote sensing measurements aim to derive detailed horizontal maps of the distribution of ice and liquid water in mixed-phase clouds. This information will be used by 3d radiative transfer simulations to estimate the impact of these cloud phase inhomogeneities on the radiative forcing and remote sensing of these clouds. Additionally, it is assumed to obtain new insight into the dynamics of ABM clouds by the combination of data from the independent measurements methods on board of Polar 5.

# References

Acarreta, J. R., Stammes, P., and Knap, W. H., 2004: First retrieval of cloud phase from SCIAMACHY spectra around 1.6 $\mu$m, Atmos. Res., 72, 89–105.

Bierwirth, E., Wendisch, M., Ehrlich, A., Heese, B., Tesche, M., Althausen, D., Schladitz, A., Müller, D., Otto, S., Trautmann, T., Dinter, T., von Hoyningen-Huene, W., and Kahn, R., 2009: Spectral surface albedo over Morocco and its impact on the radiative forcing of Saharan dust, Tellus, 61B, 252–269.

Chen, R. Y., Chang, F. L., Li, Z. Q., Ferraro, R., and Weng, F. Z., 2007: Impact of the vertical variation of cloud droplet size on the estimation of cloud liquid water path and rain detection, J. Atmos. Sci., 64, 3843–3853.

Ehrlich, A., 2009: The impact of ice crystals on radiative forcing and remote sensing of arctic boundary-layer mixed-phase clouds, Ph.D. thesis, Johannes Gutenberg University Mainz, Germany.

Ehrlich, A., Bierwirth, E., Wendisch, M., Gayet, J.-F., Mioche, G., Lampert, A., and Heintzenberg, J., 2008a: Cloud phase identification of Arctic boundary-layer clouds from airborne spectral reflection measurements: Test of three approaches, Atmos. Chem. Phys., 8, 7493–7505.

Ehrlich, A., Wendisch, M., Bierwirth, E., Herber, A., and Schwarzenböck, A., 2008b: Ice crystal shape effects on solar radiative properties of Arctic mixed-phase clouds - Dependence on microphysical properties, Atmos. Res., 88, 266–276.

Ehrlich, A., Wendisch, M., Bierwirth, E., Gayet, J.-F., Mioche, G., Lampert, A., and Mayer, B., 2009: Evidence of ice crystals at cloud top of Arctic boundary-layer mixed-phase clouds derived from airborne remote sensing, Atmos. Chem. Phys., 9, 9401–9416.

Fan, J., Ovtchinnikov, M., Comstock, J., McFarlane, S., and Khain, A., 2008: Modeling Arctic mixed-phase clouds and associated ice formation, in Proceedings of the ICCP Conference, Cancun, Mexico, July 7-11.

Fridlind, A. M., Ackerman, A. S., McFarquhar, G., Zhang, G., Poellot, M. R., DeMott, P. J., Prenni, A. J., and Heymsfield, A. J., 2007: Ice properties of single-layer stratocumulus during the Mixed-Phase Arctic Cloud Experiment: 2. Model results, J. Geophys. Res., 112, D24 202.

Garrett, T. J., Hobbs, P. V., and Gerber, H., 2001: Shortwave, single-scattering properties of arctic ice clouds, J. Geophys. Res., 106, 15.155–15.172.

Gayet, J. F., Mioche, G., Dornbrack, A., Ehrlich, A., Lampert, A., and Wendisch, M., 2009: Microphysical and optical properties of Arctic mixed-phase clouds. The 9 April 2007 case study., Atmos. Chem. Phys., 9, 6581–6595.

Gerber, H., Takano, Y., Garrett, T. J., and Hobbs, P. V., 2000: Nephelometer measurements of the asymmetry parameter, volume extinction coefficient, and backscatter ratio in Arctic clouds, J. Atmos. Sci., 57, 3.021–3.034.

Harrington, J. Y., Reisin, T., Cotton, W. R., and Kreidenweis, S. M., 1999: Cloud resolving simulations of Arctic stratus - Part II: Transition-season clouds, Atmos. Res., 51, 45–75.

Hu, Y., Vaughan, M., Liu, Z., Lin, B., Yang, P., Flittner, D., Hunt, B., Kuehn, R., Huang, J., Wu, D., Rodier, S., Powell, K., Trepte, C., and Winker, D., 2007: The depolarization attenuated backscatter relation: CALIPSO lidar measurements vs. theory, Optics Express, 15, 5327–5332.

Korolev, A. V., Isaac, G. A., Cober, S. G., Strapp, J. W., and Hallett, J., 2003: Microphysical characterization of mixed-phase clouds, Quart. J. Roy. Meteor. Soc., 129, 39–65.

Lampert, A., Ehrlich, A., Drnbrack, A., Jourdan, O., Gayet, J.-F., Mioche, G., Shcherbakov, V., Ritter, C., and Wendisch, M., 2009a: Microphysical and radiative characterization of a subvisible midlevel Arctic ice cloud by airborne observations a case study, Atmos. Chem. Phys., 9, 2647–2661.

Lampert, A., Ritter, C., Hoffmann, A., Gayet, J.-F., Mioche, G., Ehrlich, A., Drnbrack, A., Wendisch, M., and Shiobara, M., 2009b: Observations of boundary layer, mixed-phase and multi-layer Arctic clouds with different lidar systems during ASTAR 2007, Atmos. Chem. Phys. Diss., 9, 15 125–15 179.

McFarquhar, G. M., Zhang, G., Poellot, M. R., Kok, G. L., Mccoy, R., Tooman, T., Fridlind, A., and Heymsfield, A. J., 2007: Ice properties of single-layer stratocumulus during the Mixed-Phase Arctic Cloud Experiment: 1. Observations, J. Geophys. Res., 112, D24 201.

Morrison, H., Pinto, J. O., Curry, J. A., and McFarquhar, G. M., 2008: Sensitivity of modeled Arctic mixed-phase stratocumulus to cloud condensation and ice nuclei over regionally varying surface conditions, J. Geophys. Res., 113, D05 203.

Platnick, S., 2000: Vertical photon transport in cloud remote sensing problems, J. Geophys. Res., 105, 22 919–22 935.

Shupe, M. D., Matrosov, S. Y., and Uttal, T., 2006: Arctic mixed-phase cloud properties derived from surface-based sensors at SHEBA, J. Atmos. Sci., 63, 697–711.

Shupe, M. D., Daniel, J. S., de Boer, G., Eloranta, E. W., Kollias, P., Long, C. N., Luke, E. P., Turner, D. D., and Verlinde, J., 2008: A focus on mixed-phase clouds: The status of ground-based observational methods, Bull. Amer. Meteor. Soc., 89, 1549–1562.

Turner, D. D., Ackerman, S. A., Baum, B. A., Revercomb, H. E., and Yang, P., 2003: Cloud phase determination using ground-based AERI observations at SHEBA, J. Appl. Meteor., 42, 701–715.

Verlinde, J., Harrington, J. Y., McFarquhar, G. M., Yannuzzi, V. T., Avramov, A., Greenberg, S., Johnson, N., Zhang, G., Poellot, M. R., Mather, J. H., Turner, D. D., Eloranta, E. W., Zak, B. D., Prenni, A. J., Daniel, J. S., Kok, G. L., Tobin, D. C., Holz, R., Sassen, K., Spangenberg, D., Minnis, P., Tooman, T. P., Ivey, M. D., Richardson, S. J., Bahrmann, C. P., Shupe, M., DeMott, P. J., Heymsfield, A. J., and Schofield, R., 2007: The mixed-phase Arctic cloud experiment, Bull. Amer. Meteor. Soc., 88, 205.

Warren, S. G. and Brandt, R. E., 2008: Optical constants of ice from the ultraviolet to the microwave: A revised compilation, J. Geophys. Res., 113, Art. No. D14 220.

Wendisch, M., Müller, D., Schell, D., and Heintzenberg, J., 2001: An airborne spectral albedometer with active horizontal stabilization, J. Atmos. Oceanic Technol., 18, 1856–1866.

Wieliczka, D. M., Weng, S. S., and Querry, M. R., 1989: Wedge Shaped Cell For Highly Absorbent Liquids - Infrared Optical-Constants Of Water, Appl. Opt., 28, 1714–1719.